Pergamon

Journal of Atmospheric and Solar-Terrestrial Physics, Vol. 59, No. 15, pp. 1919–1943, 1997

PII: S1364-6826(97)00033-3
1364-6826/97 $17.00+0.00

Ion composition and effective ion recombination rate in the nighttime auroral lower ionosphere

C. F. del Pozo,[1,3] J. K. Hargreaves[2] and A. D. Aylward[1]

[1]Atmospheric Physics Laboratory, University College London, London W1P 7PP, U.K.; [2]Engineering Department, Lancaster University, Lancaster LA1 4YR, U.K.; [3]Physics Department, University of Wales at Aberystwyth, Ceredigion SY23 3BZ, U.K.
(*e-mail*: carlos@apg.ph.ucl.ac.uk)

(*Received* 12 *February* 1996; *in revised form* 22 *November* 1996; *accepted* 17 *March* 1997)

Abstract—We present the results of a combined study applying the Lancaster–Sodankylä model and EISCAT radar observations of the lower ionosphere during evening to early morning hours. The purpose is to derive the spectrum of incoming energetic electrons which produce the ionisation, and to determine the effective recombination coefficient and the concentrations of the positive and negative ions over the height range 70 to 120 km. This was done by combining a semiempirical 'profile-inversion' technique to estimate the spectrum of the precipitating electrons from the electron density profiles measured by the EISCAT radars, and the 35-ion Sodankylä model of the chemistry of the D and E regions. Both procedures assume chemical equilibrium conditions. It is found that, below 85 km, precipitation reduces the average ion mass at a given height by changing the relative proportions of the various ions, with the simpler molecular ions becoming dominant over the complex and hydrated ions. The same reactions occur as in the undisturbed nighttime mesosphere, and the concentrations of most cluster ions as well as most negative ions are increased by precipitation, though by less than those of the molecular ions. The effective electron–ion recombination rate is very sensitive to the energetic charged particle spectrum, and is strongly reduced by any increase of the precipitation flux at the higher energies. Above a certain threshold flux of harder precipitation (exceeding 120–150 keV), the profile of the effective recombination coefficient appears to change very little with flux, reaching values comparable to that for daytime conditions. © 1997 Elsevier Science Ltd

1. INTRODUCTION

This paper describes the Lancaster–Sodankylä ionospheric model and discusses some results obtained by combining it with EISCAT radar observations above Tromsø, in Norway. The basic aim is to investigate the chemical changes in the D and E regions during disturbed conditions, though at chemical equilibrium only (at time-scales greater than the recombination time), by combining the Sodankylä chemical model with an algorithm for the determination of the flux of precipitating particles from the measured density profiles. The 'inversion' technique is based on a method developed at the University of Lancaster (see Hargreaves and Devlin, 1990), and the chemical model was developed at the Sodankylä Geophysical Observatory (see Turunen *et al.*, 1992).

The Sodankylä chemical model gives the composition of the lower ionosphere at equilibrium. If the rate of ion pair production is assumed to be solely due to solar radiation and cosmic rays, the model applies generally to the lower ionosphere in middle latitudes, but to higher latitudes only during quiet, daytime conditions. The chemical model includes 35 ions (24 positive and 11 negative) and the 175 or so reactions occurring between them. The model may be fine-tuned to give a good representation of quiet-time electron density profiles measured by EISCAT by increasing the assumed nitric oxide concentration profile within the limits of its observed variability in the auroral region (see Burns *et al.*, 1991). Quiet-time conditions are not easily defined because residual effects from earlier disturbances may last for hours or even days. This is the case for the NO concentration which is greatly enhanced in the thermosphere during precipitation by the increase of $N(^2D)$ which reacts with O_2 to produce NO. This relatively long-lived (a few days) minor constituent is then transported into the mesosphere.

The Lancaster–Sodankylä model, on the other hand, applies to the D and E regions in the auroral zone. In addition to the solar and cosmic-ray contributions to ion-pair production, it takes into account the ionisation due to the precipitation of energetic

particles of solar and magnetospheric origin. At high latitudes, and particularly during the night, these are the main sources of ionisation. At each height, the inversion technique requires a value for the effective recombination coefficient and a value for the ratio of the concentration of negative ions to the electron density. The power profile measured by the radars is a function of both the electron density and the total negative-ion concentration in the scattering volume (see Mathews, 1978; Fukuyama and Kofman, 1980). In a recent study by Turunen (1993), the Sodankylä model has also been applied under disturbed conditions associated with the day to twilight changes in the D region during a proton precipitation event. In this case, however, the ion production rates were obtained from coincident GOES-7 satellite measurements, and then used as input to the chemical model.

Previous determinations of the flux of precipitating particles, although using similar inversion techniques, have relied on an extremely simplified chemistry and constant or averaged recombination profiles (see, for example, Hargreaves and Devlin, 1990; Burns *et al.*, 1990; del Pozo *et al.*, 1993, or other radar and satellite comparisons by Vondrak and Robinson, 1985; Kirkwood and Eliasson, 1990; Basu *et al.*, 1987; Hall *et al.*, 1992). It is very difficult experimentally to derive the effective recombination coefficient since time variations in the ion production mechanisms are complex and not completely understood, particularly below 85–90 km where cluster and negative ions are generally dominant. Various values have been obtained by several techniques (Brekke, 1975; Vickrey *et al.*, 1982; Collis *et al.*, 1986; Gledhill, 1986, and references therein) but, considering the complexity of the D region, they are not entirely satisfactory, particularly since differences of one or two orders of magnitude are not uncommon. The present method uses the chemistry contained in the Sodankylä model to obtain a more realistic value appropriate to the production rate at a given height, and this is then used in the inversion routine to obtain a better estimate of the incoming spectrum. After several iterations, the answers obtained are at least self-consistent and should therefore be reasonably accurate. A useful byproduct of the calculations is the concentration of each of the 35 ions included in the model.

The model assumes the MSIS reference neutral atmosphere complemented with a number of fixed concentration profiles for other minor neutral constituents; it considers the solar zenith dependence, and some seasonal variability and average magnetic activity effects. It does not, however, include the transient changes in the temperature of the electrons, ions, and neutrals (thus, changes in the reaction rates and cross-sections) due to the particle precipitation, enhancements in the convection electric field (i.e., collisional and Joule heating), or any drastic dynamical effects such as stratospheric/mesospheric warmings. Also, it does not consider the changes in the concentration of some relevant neutral constituents due to dynamical effects in the neutral atmosphere (mainly wind transport and diffusion) at the longer timescales, or the sporadic presence of heavy metallic ions below 95 km due to meteor ablation. We plan, in the near future, to include most of these 'second-order' effects (which may, however, play a very important role) by coupling the UCL-Sheffield 3-D global thermosphere–ionosphere model together with an improved version of the chemical equilibrium model. For a concise review of the various processes occurring in the high-latitude lower ionosphere, and the different temporal and spatial scales involved, see, for example, Schunk and Sojka (1995).

In Section 2, we introduce the main assumptions of our model, giving a brief description of both the Sodankylä chemical model and the algorithm for the inversion of the observed density profiles. In Section 3 we introduce the experiments and the observing conditions, and in Section 4 we discuss the model results and comparisons. Finally, in Section 5, we present the conclusions of the study.

2. LANCASTER–SODANKYLÄ MODEL

This is a model of the disturbed D and E regions which combines the Sodankylä ion chemistry model with a procedure to estimate the spectrum of precipitated particles by inverting the electron density profiles measured by the EISCAT radars. It therefore consists of two main parts: (1) the Sodankylä ion chemistry model (see Burns *et al.*, 1991; Turunen *et al.*, 1992), and (2) an inversion algorithm which applies the Rees semi-empirical approximation to the normalized energy dissipation function for an isotropic pitch angle distribution of precipitating particles (see Rees, 1989, pages 35–45; Fuller-Rowell and Evans, 1987; Basu *et al.*, 1987; and also Jasperse and Strickland, 1981, for some rigorous definitions). The structure of the Lancaster–Sodankylä model is shown in the block diagram of Fig. 1. At each time step, it determines the MSIS neutral atmosphere and the solar and cosmic-ray production rates, and estimates the electron precipitation flux in iteration with the Sodankylä chemical model. In this manner, by getting the best fit to the measured electron density profiles, it obtains the height profiles of the various ion-concentrations, the effective ion recombination

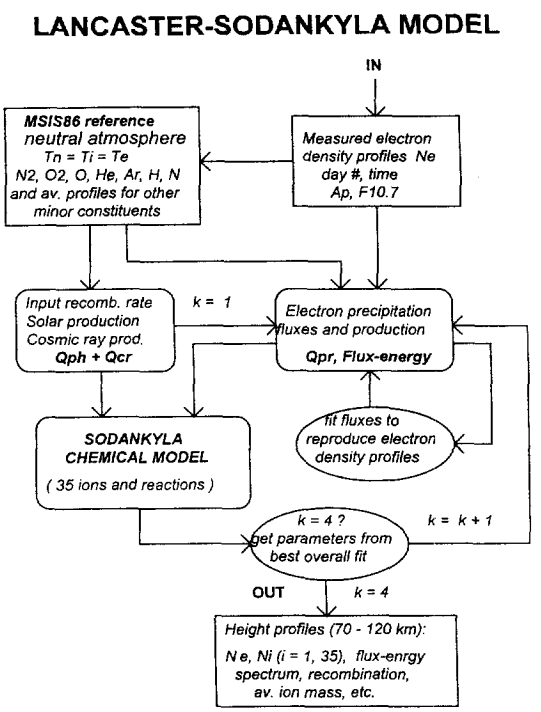

Fig. 1. Schematic view of the Lancaster–Sodankylä model. It involves two main iteration loops, one in the profile 'inversion' block for the estimation of the precipitation fluxes from the measured electron densities, and the other which combines the chemical equilibrium model and the inversion algorithm repeating all the model calculations four times to obtain a better estimate of α_{eff} at all heights.

coefficient, and the flux-energy spectrum of the precipitating electrons. The procedure works on a 200 m height grid.

2.1. *Sodankylä chemical model*

This model includes 35 ions (24 positive and 11 negative) and the 175 reactions likely to occur between them. In addition to the five main positive ions in the D and E regions (O^+, O_2^+, N_2^+, NO^+, and O_4^+), it includes 11 negative ions (O^-, O_2^-, O_3^-, O_4^-, OH^-, CO_3^-, CO_4^-, NO_2^-, NO_3^-, NO_3^-*, and HCO_3^-), proton hydrates ($H^+(H_2O)_n$, $n = 1$–8), NO^+ hydrates ($NO^+(H_2O)_n$, $n = 1, 2, 3$; $NO^+(H_2O)_nN_2$, $n = 1, 2$; and $NO^+(H_2O)_nCO_2$, $n = 1, 2$), and other cluster ions ($NO^+(N_2)$, $NO^+(CO_2)$, $O_2^+(H_2O)$, and $H_3O^+(OH)$). The model uses the MSIS86 reference neutral atmosphere (Hedin, 1987), with extrapolation below 85 km, for the temperatures (with $T_n = T_i = T_e$) and the concentrations of N_2, O_2, O, H, Ar, He and N. It allows for some solar and magnetic activity effects through the F10.7 and *Ap* indices. The model also includes a number of fixed concentration profiles for other minor constituents such as O_3, CO_2, OH, NO_2, NO, H_2O, HO_2, and $O*_2$, obtained from various sources — see Fig. 6 in Burns *et al.* (1991).

2.1.1. *Ionisation by solar radiation and cosmic-rays.* At each step the model calculates the production rate due to solar radiation and cosmic rays, using reaction rates and absorption/ionisation cross-sections taken from a wide range of sources in the literature. Under quiet conditions the main sources of ionisation in the D region between 60 and 85–90 km height, and the E region from 85–90 to 130 km height, are the X-rays and the EUV parts of the solar radiation and the galactic cosmic rays. The cosmic rays are dominant below 65 km. Whereas X-rays ionise all constituents in the D and E regions, their relative importance is very small and is significant only during solar maximum conditions (as in this study). This leaves the EUV range as the principal agent in the formation of the lower ionosphere by the ionisation and dissociation of the molecular oxygen, mainly in the E region, and the ionisation of the nitric oxide, mainly in the D region, by the strong Lyman-α and Lyman-β fluxes (at 121.6 nm and 102.6 nm). The photoionisation rate is calculated as:

$$Q_{jph} = \int_\lambda d\lambda\, \eta_j(\lambda)\sigma_j(\lambda)n_{nj}(z)I_\infty(\lambda) \exp[\Sigma_k \sigma_k(\lambda)\int_z^\infty dh\, n_{nk}(h)Ch(h,\chi)] \quad (1)$$

for solar zenith angle χ, at the height z, for neutral constituent j of concentration n_{nj}, and where I_∞ is the intensity of the solar radiation at wavelength λ outside the atmosphere (we consider 50 bands, between 5 and 140 nm). The Chapman function $Ch(z, \chi)$ accounts for the Earth's curvature and it is calculated numerically, and σ_k and η_k are the absorption cross-section and the photoionisation efficiency for neutral component k, respectively. The scattered Lyman-α flux is represented by the empirical approximation given by Thomas and Bowman (1986), and in a similar way the diffuse Lyman-β from the curves in Strobel *et al.* (1974). Cosmic rays, on the other hand, provide the dominant source of ionisation in the lower mesosphere, stratosphere and troposphere, and pair production has been parameterized (see Brasseur and Solomon, 1986, p. 329) as a function of latitute, altitude and solar activity level. For latitudes greater than 53°, we have (in S.I. units): $Q_{jcr}(z) = 1.44 \times 10^{-17} n_{nj}(z)$ for solar maximum conditions, whereas for solar minimum we have, $Q_{jcr}(z) = (1.44 \times 10^{-17} + 4.92 \times 10^{-18})$ $n_{nj}(z)$. In these equations, $n_{nj}(z)$ is the vertical concentration of neutral species j, and ionisation is basi-

cally the result of the interaction with the two main atmospheric constituents N_2 and O_2.

2.1.2. *Chemical equilibrium.* Below 120–130 km, we may assume chemical equilibrium and *in-situ* charge neutralization because the recombination processes ensure that the chemical lifetimes of the ions are short with respect to changes due to transport processes. Thus, for each ion species, the steady-state balance between production and loss can be written as an equation, and the totality may be expressed as a group of equations in matrix form:

$$\langle \mathbf{R}(\mathbf{N}) \rangle \cdot \mathbf{N} + \mathbf{P}(\mathbf{N}) = 0 \tag{2}$$

where **N** is the vector formed from the different ion concentrations, $\langle \mathbf{R} \rangle$ is the matrix containing as its diagonal the loss rates of each ion, and as its non-diagonal elements the production rates due to chemical reactions between ions and neutrals. Vector **P** contains as its elements the production rates due to the various ionisation sources, as well as the formation of negative ions by attachment to neutrals. The group of equations in equation (2) is solved using the Newton–Raphson method (see Turunen *et al.*, 1992). Also, writing explicitly the equilibrium continuity equation for electrons, we have (Brasseur and Solomon, 1986, p. 321):

$$\frac{\mathrm{d}}{\mathrm{d}t} n_e = \frac{1}{(1+\lambda_-)} [\Sigma_j Q_j - n_e \Sigma_j (\alpha_{Dj} + \lambda_- \alpha_{Ij}) n_j^+] \to 0 \tag{3}$$

where α_{Dj} and α_{Ij} are the total electron–ion and the ion–ion recombination rates for ion j, and λ_- is the ratio of total negative ion-concentration to n_e. From charge neutrality $\Sigma_j n_j^+ = n_e + \Sigma_l n_l^-$, and the effective recombination rate is usually defined by:

$$\alpha_{\mathrm{eff}} = \Sigma_j (\alpha_{Dj} + \lambda_- \alpha_{Ij}) \delta_j^+ . \tag{4}$$

The ratio $\delta_j^+ = n_j^+ / \Sigma_j n_j^+$ is the fractional concentration of positive ions j. At equilibrium, $\alpha_{\mathrm{eff}} = q_{\mathrm{tot}} / n_e^2$ where $q_{\mathrm{tot}} = Q_{\mathrm{tot}} / (1+\lambda_-)$ is the total electron production rate ($Q_{\mathrm{tot}} = \Sigma_j Q_j$ is the total ion-pair production rate), and the effective recombination coefficient determines the rate of loss of the electron–ion pairs, and thus the equilibrium electron density. It is a function of the collision cross-sections, the distribution functions of the collision partners, the reduced masses and temperature, as well as of the relative concentrations of the positive ions and of the negative ion ratio. At equilibrium this coefficient is indeed independent of the electron density, but different equilibrium compositions may be reached at different times depending on the relative abundance of the various ions. The radical difference between the daytime and the quiet nighttime compositions and recombination coefficients, as well as during other sharp transitions in the solar production (sunset, sunrise, eclipses), must be kept in mind. Our study shows that the night-to-early morning composition also changes with the spectrum of precipitating particles, and this may give an apparent dependence on the electron densities. We also find that above a certain flux of harder precipitation there is a unchanging, 'saturation' recombination profile, very similar to the daytime conditions. The LS model determines the equilibrium ion composition associated with the observed density profile at each time, and in order to insure the independence of two consecutive determinations we consider integration times greater than the recombination times.

2.2. *Precipitation production rate and flux spectrum*

At high latitudes, particularly during nighttime or disturbed conditions, the main source of ionisation is the precipitation of energetic particles of solar and magnetospheric origin. The incoming particles ionise the atmospheric constituents, producing secondary electrons which are equivalent to the photoelectrons produced by solar radiation, and the total production rate is simply the sum of the pair production rates due to particle precipitation, solar radiation and cosmic-rays.

2.2.1. *Calculation of production rate from an assumed particle influx.* Following Rees (1989) (p. 40), the rate of collisional ionisation $q(z,E)$ between neutrals and a flux of monoenergetic particles is given by:

$$q(z,E) = K(z,E)\Phi(E) \tag{5}$$

with

$$K(z,E) = \frac{E}{R \Delta \epsilon_o} \Lambda(\zeta/R) \rho(z) \tag{6}$$

where $\Phi(E)$ is the incident flux (per unit time per unit area normal to the z-axis) at energy E, $\Delta\epsilon_o$ is the energy per ionisation, which is about the same for all major species (≈ 37 eV), and $\rho(z)$ is the atmospheric mass density. The function $\Lambda(\zeta/R)$ is in general the normalized energy dissipation function (see Basu *et al.*, 1987), and in the case of electron precipitation it may be approximated by Rees' lambda function (Rees, 1963) obtained in laboratory experiments. The maximum penetration range, R, for a beam of initial energy (E), is given (Rees, 1989) by:

$$R = 4.3 \times 10^{-7} + 5.36 \times 10^{-6} E^{1.67} \tag{7}$$

where R is given in grams per square centimetre and the energy expressed in keV, ζ is the atmospheric depth

at height z, and R is the atmospheric depth corresponding to the deposition height at which the beam has deposited all its energy. The existence of a penetration depth means that for each incident particle there is some altitude, depending on its initial energy, below which it produces no ionisation whatsoever. In consequence, we expect ionisation below 90 km to be due entirely to electrons whose initial energy exceeds about 24 keV, that below 80 km to energies above 70 keV, and that below 70 km to energies above 170 keV. Over the range 10 to 200 keV, the penetration height reduces by about 7 km for each doubling of the initial energy. We are not considering the additional ionisation at lower heights caused by bremsstrahlung X-rays from the deceleration of the high energy electrons. The associated ionisation rate is almost constant over nearly 50 km below the height of maximum ionisation from the primary monoenergetic beam, but thousands of times smaller (see Berger *et al.*, 1974).

Although energetic electron precipitation is generally the dominant source of ionisation in the nighttime auroral region, in some cases proton precipitation may be important or dominant. Then the ionisation is the sum of the pair production by the electrons and by the ions, with the appropriate approximations for the range and the lambda function (the Bragg curve, Rees, 1989, p. 50). The production rate $q(z,E)$ for monoenergetic particles may be convolved with the energy spectrum of precipitation to obtain the total ionisation rate $Q(z)$ (pair-production per cubic centimetre per second), and it basically covers the three major constituents N_2, O_2, and O. In the periods discussed here, however, ionisation was produced by fluxes of energetic electrons which generally originate in the central plasma sheet and are associated with diffuse auroral precipitation. They generally follow the power law spectrum with no evidence of acceleration along the magnetic field (see Rostoker *et al.*, 1985); only around the Harang discontinuity region would the incoming electrons show signs of parallel acceleration.

The isotropic, but otherwise arbitrary, incident flux is decomposed into a sum of individual beams over 26 energy bands, in the range between 3 and 380 keV for electrons penetrating into the E and D regions. For instance, assuming a discrete set of heights, the total ion-pair production rate due to particle precipitation may written as:

$$Q(z_j) = \pi \Sigma_i K(z_j,E_i) F(E_i) \Delta E_i \qquad (8)$$

where $Q(z_j)$ is the total ionisation at height z_j and $K(z_j, E_i)$ is proportional to the energy deposition function at height z_j for the incoming beam at energy E_i. The sum is performed over energies with corresponding penetration ranges R greater than or equal to ζ. The downward flux of incident electrons per unit energy per unit time per unit area per steradian (the differential flux, or flux-energy, spectrum) is, in general, given by

$$F(E) = \Phi(\Delta E)(E/E_o)^{\gamma} e^{-E/E_o}. \qquad (9)$$

E_o (or more exactly $E_{o(i)}$) is the characteristic energy in the band E_i and width ΔE_i. Different characteristic energies will indicate the presence of uncorrelated electron precipitation in the corresponding energy bands. In the present study we are assuming the 'plain' exponential dependence (with $\gamma = 0$) in all bands. Only in the case of very narrow bandwidths, no *a priori* assumption on the spectral distribution of the incoming particles needs to be made. This is equivalent to the decomposition of an arbitrary flux into a sum of monoenergetic beams (see Rees, 1963).

2.2.2. *Inversion of electron density profile.* Different methods are available to determine the flux spectrum from equation (8). Most of these methods use a standard matrix inversion and least squares fit technique (as in Barouch, 1980; Kirkwood, 1988; and also Vondrak and Baron, 1977). Our method is simply to adjust the spectrum by trial and error until the electron density profile computed from it is a sufficiently close match to the observed profile. After a number of iterations, we may also apply a least-squares fit to the ensemble of points to smooth the overall result; the fitting is weighted by the errors in the inferred fluxes, derived from the errors in the measured densities. Thus, we wish to adjust the flux in each of the energy bands so as to match the observed electron density profile. Although the height of maximum production rate as a function of initial energy is well known (e.g. Hargreaves, 1992, p. 216), even a monoenergetic flux creates significant ionisation over a considerable height range. For initial energies between 10 and 200 keV, ionisation occurs at a rate of at least half the maximum over a height range of about 10 km. The distance between the points representing the flux at one energy therefore affects the ionisation over many heights, and it is not obvious what relationship between energy and height should be chosen to achieve the best convergence. After some trials, the formula selected is:

$$E(z) = 4 \times 10^5 e^{-0.101z} \qquad (10)$$

where $E(z)$, in keV, is the energy 'corresponding' to altitude z in km. Taking all sources of ionisation (particles, photoionisation and cosmic rays), and the effective ion-recombination profile (α_{eff}) into account

we calculate the electron density profile (n_e') to be compared with the observations (n_e). The process begins with an initial guess for the flux $F'(z)$ ($\equiv F'(E(z))$) at each height; at the next iteration the fluxes are modified according to $F(z) = F'(z) \times (Q(z)/Q'(z))$. The flux $F(E_i)$ at each energy band, with $E(z_j) \leq E_i \leq E(z_{j+1})$, is obtained from interpolation onto the calculated flux-height grid corresponding to the density profile. Then, we calculate a new estimate of the total ionisation rate and the process is repeated until the calculated profile is within a stated tolerance (generally set to 5 or 10%) of the observed one. We have also applied the matrix inversion/least-squares technique to equation (8) for some of the data; the results compare reasonably well with our point-by-point determinations at the lower energies where the concentration of energy bands is higher. At higher energies (> a few tens keV), however, the matrix-inversion estimates are generally unstable, showing large oscillations in the resulting spectrum. This problem does not arise in our method unless the data are of poor quality, or in the presence of narrow layers of enhanced precipitation.

3. EXPERIMENTS

The data analysed in this study are from several multibeam EISCAT experiments carried out by the Space Environment Group at Lancaster University during 1990, 1991 and 1992, with the support of the EISCAT group at the Rutherford Appleton Laboratory. They consisted of periods of 6 to 12 h of D and E region observations during evening to early morning hours, at 1 km range resolution over 70 to 88 gates (starting at 68–70 km height), and time resolution between 2 to 10 s. The experiments included the simultaneous operation of both the tristatic UHF (934 MHz) and the VHF (224 MHz) radars. We will not go into the details of the experimental configurations or the system parameters. The EISCAT system has been extensively described in the literature (see also del Pozo *et al.*, 1993 for a description of similar experiments). In this study we only use data from the tristatic system; this includes backscatter measurements of the density profile above Tromsø either along the vertical, or parallel or nearly-parallel to the magnetic field. It also includes the passive reception by the other two antennas at Kiruna and Sodankylä from the intersection volume centred at a fixed height in the F-region (at 300 or 350 km). From the tristatic observation we can obtain the $\mathbf{E} \times \mathbf{B}$ drift, and hence the electric field **E**. The experiments discussed here were performed on:

- (A) 26–27 March 1992, from 16:00 to 05:50 UT (LT = UT + 1.2 h, at Tromsø),
- (B) 27–28 September 1991, from 18:00 to 04:30 UT, and
- (C) 13–14 March 1991, from 18:10 to 05:30 UT.

All experiments were carried out during the first part of the current solar maximum. The starting and ending daily values of F10.7 for periods (A), (B), and (C) were, respectively, 185.1 and 177.9, 201.6 and 178.7, and 153.7 and 195.5. Our model assumes the reference irradiances given by Rees (1989)(appendix 2) for F10.7 = 243.0 (see also Roble, 1995). The solar spectra at any other value of F10.7 are estimated by scaling the reference spectrum by the ratio F10.7/243.0. In this study, however, the solar flux input is of little relevance because the observing periods fell mainly in the night sector. During period (A) the magnetic activity was moderate and associated with daily *Ap* values of 12 and 11, and 3-hourly *Kp* values of 3.7, 2.7, 2.7 and 2.0. Electric fields were also moderate; during some intervals between 00:00 and 03:00 UT the field strength exceeded 25 mV/m. On the other hand, most of period (B) corresponded to disturbed magnetic conditions with high daily *Ap* values of 48 and 40, and high 3-hourly *Kp* values (5.0, 3.3, 4.3, and 5.0). The electric field was also strong and its amplitude was consistently above 25 mV/m during the whole period. Finally, period (C) went from moderately high to low magnetic activity conditions with daily *Ap* equal to 27 and 7, and moderate 3-hourly *Kp* values (1.3, 0.3, 3.0, and 2.3). The electric field during this period was generally weak (below 20–25 mV/m), with the exception of the interval from 00:00 to 03:00 UT, as in period (A).

In Fig. 2 we present the raw electron density measured by the EISCAT UHF radar at Tromsø against height and Universal Time, and the flux-energy spectrum calculated by our combined model against energy and Universal Time. The electron density is expressed in cm^{-3} and the flux spectrum in /keV/s/cm^2/sr. Figure 2(a) shows the data and derived fluxes for 26–27 March 1992 (from 16:44 UT), Fig. 2(b) for 27–28 September 1991, and Fig. 2(c) for 13–14 March 1991. The integration time is 1 min throughout, and some localized features in the electron density plots may not be clearly matched by signatures in the flux spectrum plots. This is an artifact due to the smearing of the colour pixels along both the x and y directions. If n_e is the actual electron density, the raw density $\bar{n}_e$ is given by:

$$\bar{n}_e = 2n_e \frac{1 + 2\lambda_-}{(1+\alpha^2)[\alpha^2 + 2(1+\lambda_-)]}. \qquad (11)$$

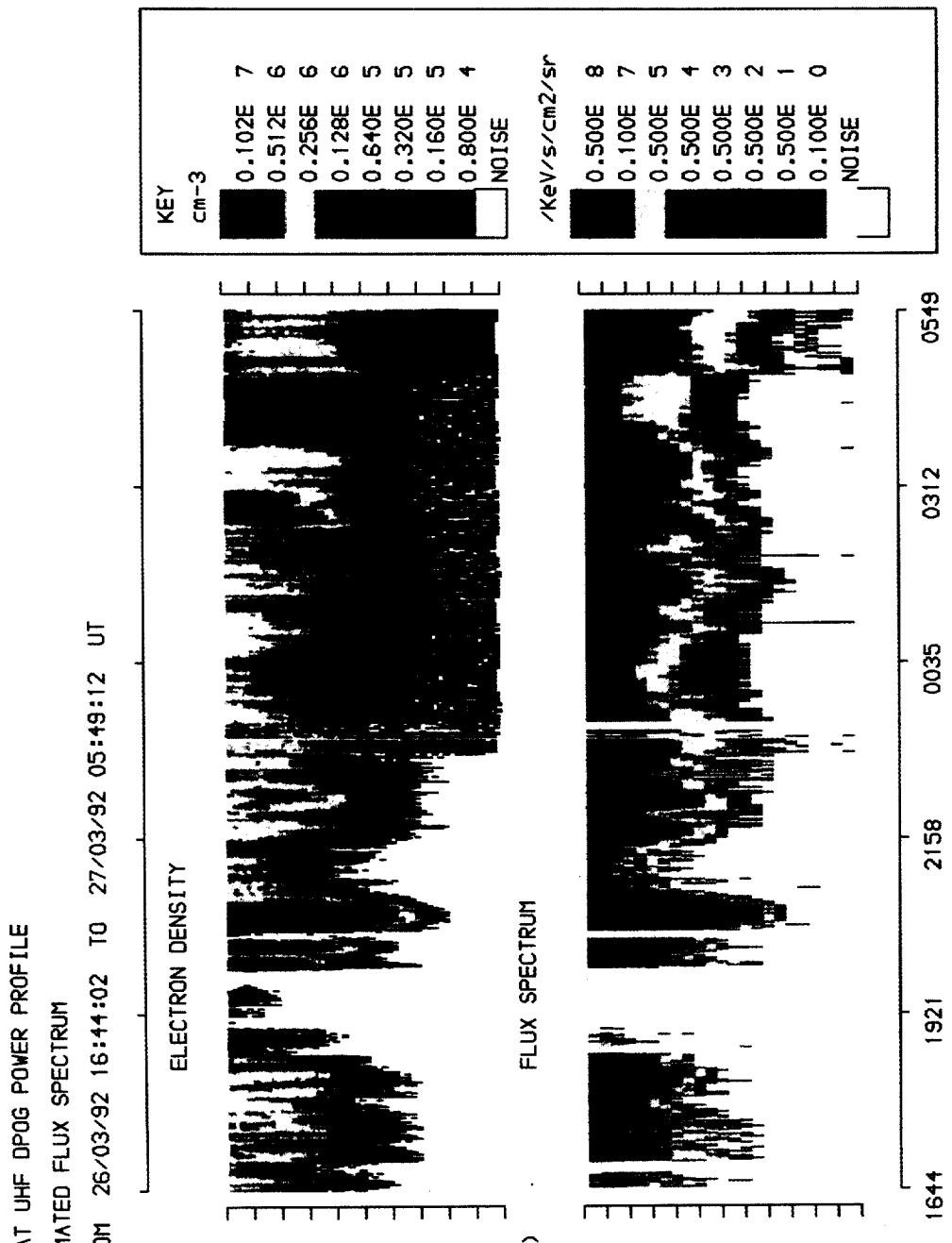

Fig. 2. Upper panel, electron density measured by the EISCAT UHF radar at Tromsø, as a function of height and Universal Time. The colour-coded scale is in cm^{-3}. Lower panel, flux-energy spectrum obtained with our combined model, as a function of energy and Universal Time. The colour coded scale is in /keV/s/cm^2/sr. Figure 2(a) corresponds to 26–27 March 1992, Fig. 2(b) to 27–28 September 1991, and Fig. 2(c) to 13–14 March 1991.

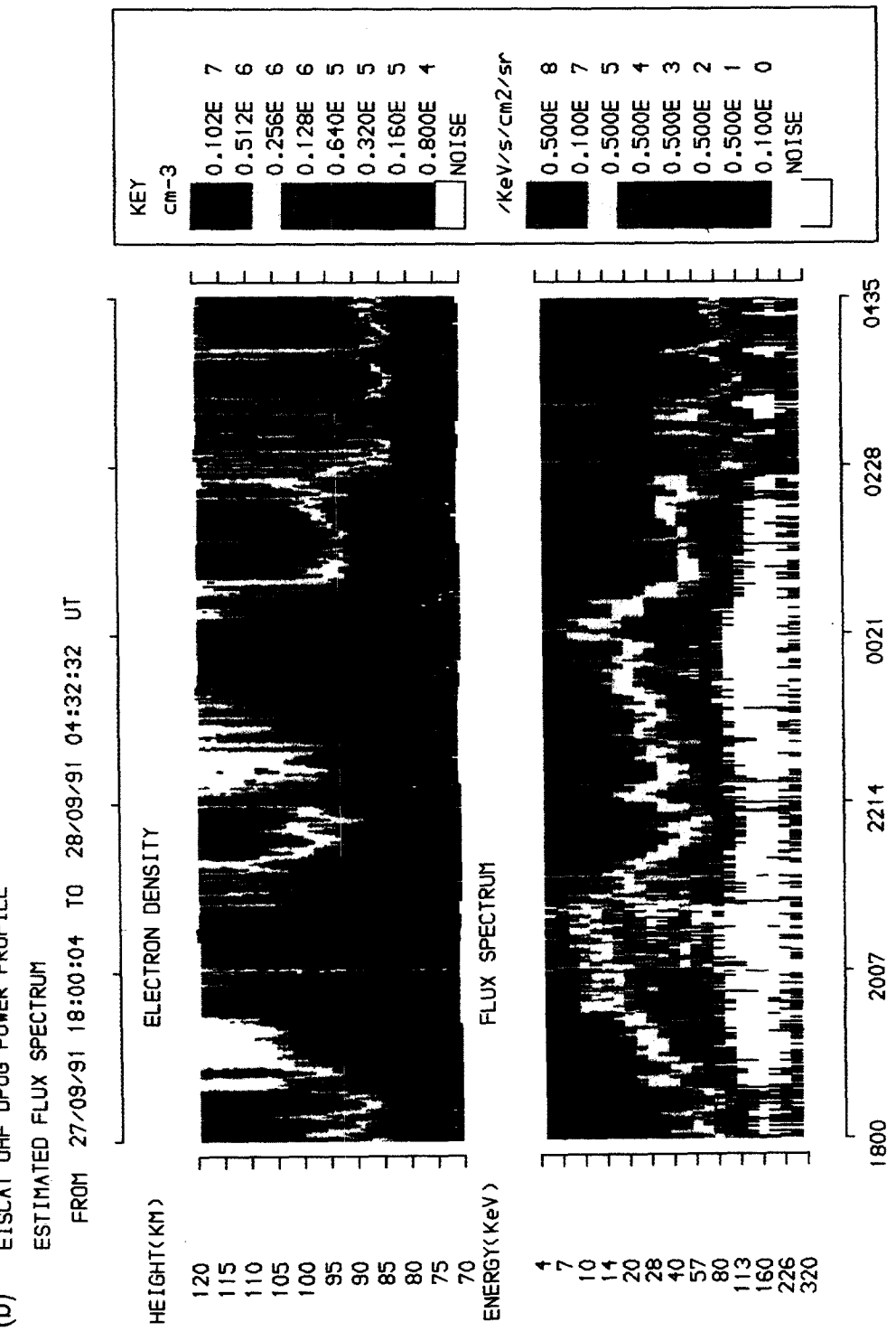

Fig. 2—*continued.*

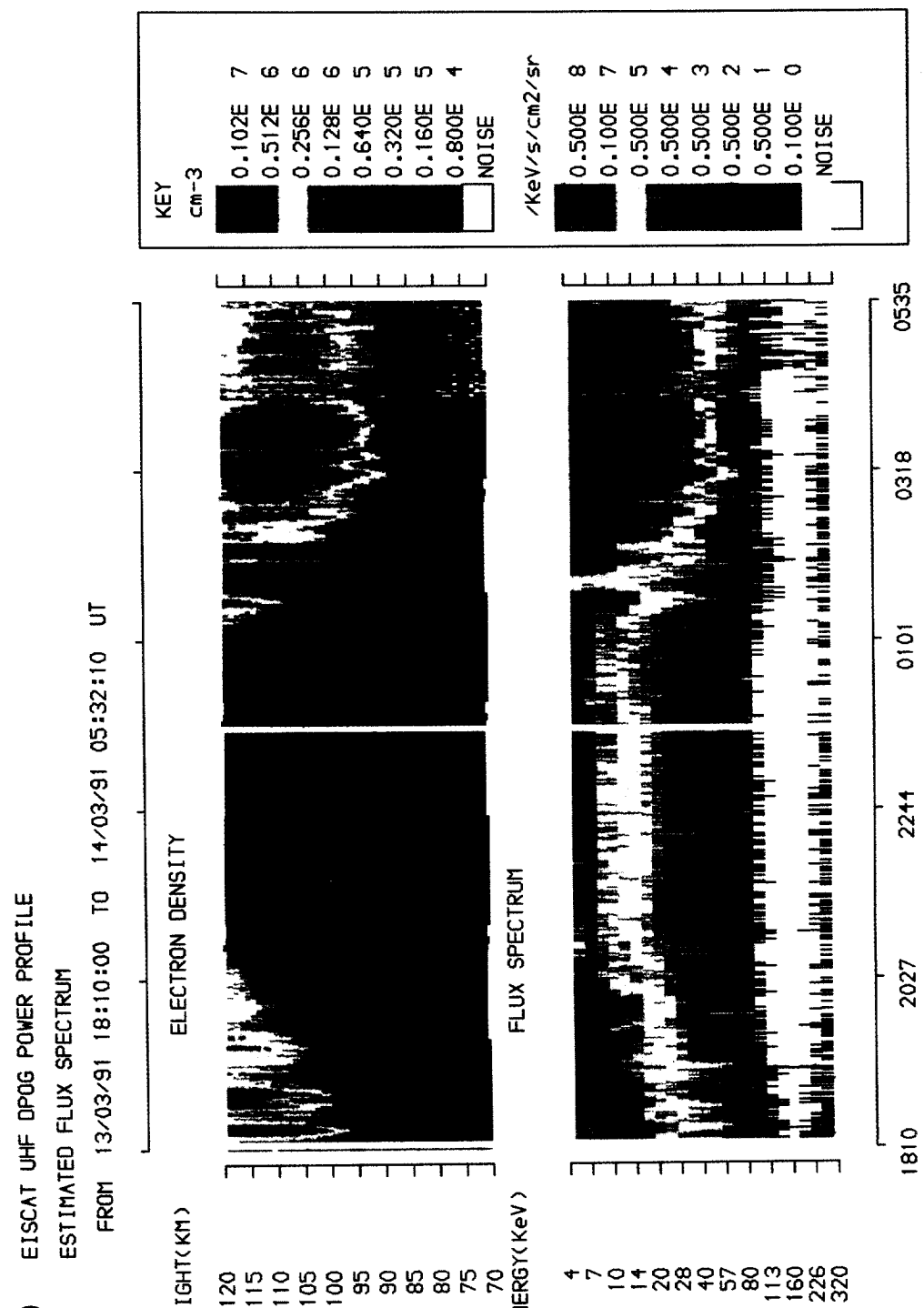

Fig. 2—*continued.*

This equation was obtained by considering the presence of negative ions in the radar scattering volume (see Mathews, 1978; Fukuyama and Kofman, 1980). The Debye length dependency $\alpha^2 = k^2\lambda_{De}^2$ ($= (6.9 \times 4\pi/\lambda_R)^2(T_e/n_e)$, with T_e given in °K, n_e in cm^{-3}, and the radar wavelength $\lambda_R = 32$ cm) cannot be neglected for densities smaller than $10^4\,cm^{-3}$, which is generally the case below 80 km. The ratio of the raw electron density to its true value increases with the concentration of negative ions, and it may significantly differ from unity, but only below 80 km height, reaching a maximum value of two. We notice that the raw density is a nonlinear function of $\bar{n}_e$, through both the α and the λ_- terms. The best estimates of the true electron density, as well as of the concentrations of the 35 ions considered in the model, are obtained by comparing the measured raw densities with an estimate of these at each iteration of the main loop in the model calculations (see Fig. 1).

The determinations of the flux-energy spectrum correspond to 26 energy bands for an equal number of density heights, every 2 km between 70 and 120 km. Three point averages have been taken of the original 1 km resolution profiles, in order to improve the stability of the inversion algorithm (particularly at lower altitudes). The bands are centred at energies E_i (keV) = 3.5, 5.9, 7.1, 8.4, 10.0, 11.9, 14.1, 16.8, 20.0, 23.8, 28.3, 33.6, 40.0, 47.6, 56.6, 67.3, 80.0, 95.1, 113.1, 134.5, 160.0, 190.3, 226.3, 269.1, 320.0, and 380, a logarithmic progression in which the energy doubles every 4 steps. Our observations involve, typically, heights above 120 km but down to only 70–69 km, and this corresponds to a reliable determination of the flux spectrum between 3 and 270 keV. The bandwidths are simply defined by the points halfway between the band centres.

3.1. *Experimental and model errors*

The relative error in the raw density is a function of the signal to noise ratio in the measuring process, divided by the square root of the number of independent determinations, N_I, which are averaged together over the chosen integration time:

$$\frac{\Delta n_e}{n_e} = \frac{1}{\sqrt{N_I}}(1 + SNR^{-1}). \tag{12}$$

For integration times of the order of 10 s to 1 min, this relative error is typically smaller than 10 to 5%, but it rapidly increases as the background ionisation decreases, and the ability of the system to discriminate between the signal and the embedding noise is reduced. This is generally the case during nighttime and lower altitudes. The minimum value for the electron density that can be measured by the EISCAT radar at UHF is of the order of $10^3\,cm^{-3}$, and raw densities as low as $3\text{–}5 \times 10^3\,cm^{-3}$ must be reliable. Stable determinations at these levels correspond to individual measurents with a SNR greater than ~2%, and typical post-integration errors smaller than 20% on the 1 to 5 min scale. Usually, at heights lower than 80 km, ionisation by secondary X-rays from the deceleration of the energetic electrons may generate a maximum background electron density smaller than $10^3\,cm^{-3}$, and this is below the noise level in the radar determinations. Referring to Berger *et al.* (1974), and to Fig. 3.3.3 from Rees (1989) (p. 41), in order to produce secondary X-ray ionisation greater than $10^3\,cm^{-3}$, for typical recombination coefficients in the range $10^{-6}\text{–}10^{-4}\,cm^3/s$ (below 85–80 km), we require secondary production rates of $Q_s \approx 1\text{–}10^2/cm^3/s$, and thus primary precipitation fluxes greater than $10^8/cm^2/s$ at all energy bands (since primary production is $\approx 10^4 \times Q_s$). Most of the time, the integral precipitation flux decreases sharply with increasing energy and is smaller than $10^8\text{–}10^7/cm^2/s$ in the 1 to 10 keV energy range, and smaller than 10^4 for energies greater than 100 keV. It is, therefore, in the presence of very strong fluxes in the 50–100 keV range (a double humped spectrum) that we would expect to observe ionisation from secondary X-ray production.

When the measured densities are above the background noise, the estimated fluxes should be fairly accurate. Very small fluxes (smaller than $0.1/keV/cm^2/s/sr$, say), however, tend to produce weak, irregular ionisation which is difficult to distinguish from the noise level in the radar determinations. Greater fluxes are probably real, so far as they are related to regular, 'well behaved' (stable signal-to-noise ratios, greater than 2–5%), measured density profiles, matched closely by the model results. If there were substantial errors in the measured electron density, the inversion method may fail or produce unrealistic shapes in the flux spectrum with large oscillations between adjacent energy bands. In our point-by-point determination the quality of the estimated flux is a function of the error in the observed density. Actually, from equation (8), and keeping all the other factors unchanged, the error in the flux is twice the error in the density. This generally worsens at lower altitudes (for the high-energy side of the spectrum), but in the case of 'well behaved' observations it is less than 10–20%, and in any case smaller than 40%. The build-up of secondary maxima — much greater than 0.1 — at the higher energies may be real provided that they involve more than 2 or 3 energy bands, but excluding the very last two bands (at 320 and 380 keV).

An unrealistic recombination coefficient profile

could also be a source of error, but this is unlikely in the case of our model as it estimates the profile in a consistent manner, using the electron density data and a sophisticated chemical model. There is, however, the possibility that the chemical model may underestimate the importance of some ions and reactions, due to the uncertainties in a number of parameters, and on the background neutral concentrations — especially for the minor constituents. A more fundamental disagreement could arise if the Rees semi-empirical approximation to the normalized energy deposition function for the electrons (or the one derived for the ions using the Bragg curve) were not justified. This is thought to be unlikely, since the approximation has been broadly applied and seems to be well adapted for precipitating particles over a wide range of energies. This is particularly so for electrons during diffuse auroral conditions and, with some restrictions, also for proton precipitation events producing ionisation below 120–130 km, the E-region peak (see Basu *et al.*, 1987; Hall *et al.*, 1992).

4. MODEL RESULTS AND COMPARISONS

We consider the results of our model and discuss a number of Figures which display side by side the input densities and the fitted profiles, the resulting flux-energy spectra, and the inferred effective recombination coefficients. From within the periods in Fig. 2 we have chosen a number of events at various times, and looked in detail at their evolution over 1 and 5 min integration times.

4.1. *Flux spectrum*

In Fig. 3 we show the results of the model for a set of five 1 min runs from 18:17 to 18:21 UT (19:29–19:33 LT) on 27 September 1991, in the presence of relatively high fluxes of hard electron precipitation. We have plotted the decimal logarithm of the differential flux for the energy bands between 3 and 320 keV, the height profiles of the decimal logarithms of the measured and model densities, and the recombination coefficient multiplied by 10^8. We may notice the good agreement between the input density profiles and those generated by the model. Roughly, differential fluxes smaller than $0.1/cm^2/st/s/keV$ (horizontal line in the flux spectrum plot), for energies greater than 100–200 keV, correspond to electron densities, below 80 km height, of less than $10^3\,cm^{-3}$. The variability in the fluxes at the high energy end of the spectra is in fact due to the poor SNR of the electron density measurements at lower altitudes. Most spectra in Fig. 2(b) and Fig. 2(c), and in some intervals of Fig. 2(a), show what appear to be narrow Maxwellian distributions at very low energies, and then a broader, nearly Maxwellian, distribution with a pronounced tail at the middle energies. In addition, there is often what appears to be a distinctive spectral component at the higher energies, which may be responsible for the ionisation at the lower altitudes, and corresponding to differential fluxes greater than 0.1 (see Figs 3 and 4). The existence of such a high energy component is very puzzling; a separated spectral signature of the kind is typical of radiation belt spectra but not of precipitating electrons. Due to the high variability of our low altitude/high energy determinations, and despite the fact that they appear to be associated with ionisation rates above the noise level, we will not at this time set any strong claim on the possible origin of the corresponding spectral signatures, neither will we completely rule out the possible effects of bremsstrahlung X-rays.

Could this separated high-energy population also originate in the central plasma sheet (CPS), but with similar characteristics to those of the discrete precipitation from the boundary plasma sheet (BPS)? If so, lower-altitude ionisation may be the result of electrons from the outer edge of the radiation belts with energies above some sharp cutoff in the range 20 to 60 keV (Kirkwood and Eliasson, 1990), or at even higher energies as seems to be indicated from our determinations. It may be the position of the trapping boundary for high energy electrons within the otherwise continuous plasma sheet region which determines the equatorward boundary of discrete precipitation, and not the transition between CPS and BPS regions (Winningham *et al.*, 1975). The very dynamic nature of the trapping boundary could thus explain the variety of spectral signatures which we obtain as well as the presence of a separated population of very energetic electrons at the latitude of Tromsø. We hope to address this question properly in a future study, applying higher quality data from stronger ionisation below 80 km.

In Fig. 4, despite the strong noise in the measured densities (particularly at the lower altitudes), both the data and the fitted profiles show the presence of enhanced ionisation between 95 and 90 km. This corresponds to the ionisation E layer which can be seen in Fig. 2(b); it lasted almost 2 h (from 19:00 to 21:00 UT), gradually reducing its height from 95 to 85 km. The recombination profiles do not show any signs of this and are very similar to those in Fig. 3. On the other hand, the particle spectra are clearly different and the ionisation layer is associated with well defined features breaking into the spectra in the 25 to 50 keV energy range. The 'intrusions' are sharper at times, and fall

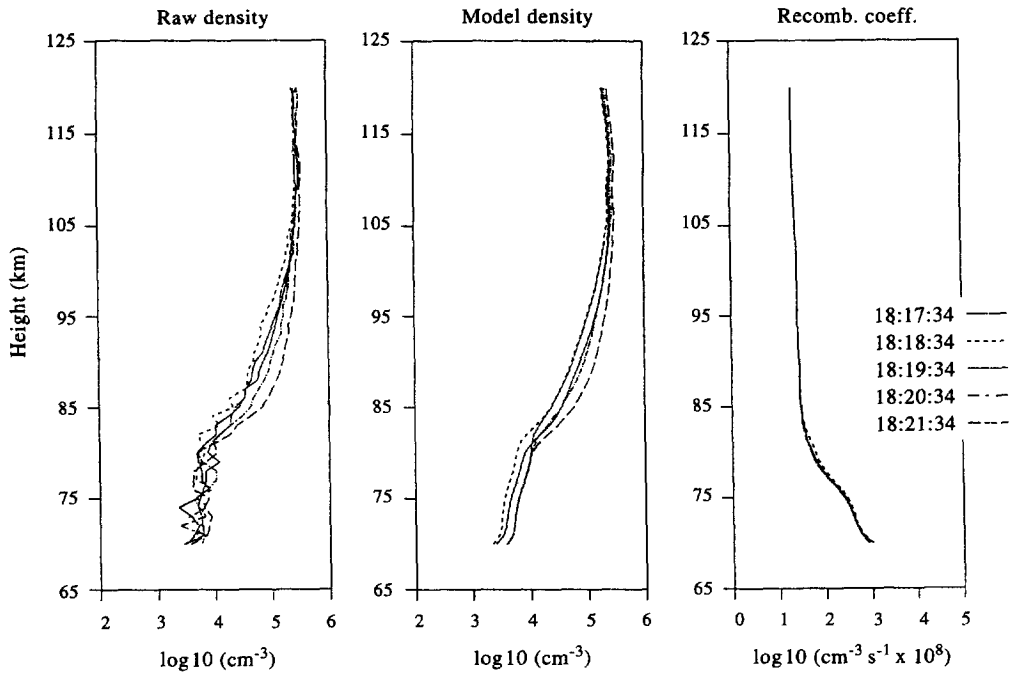

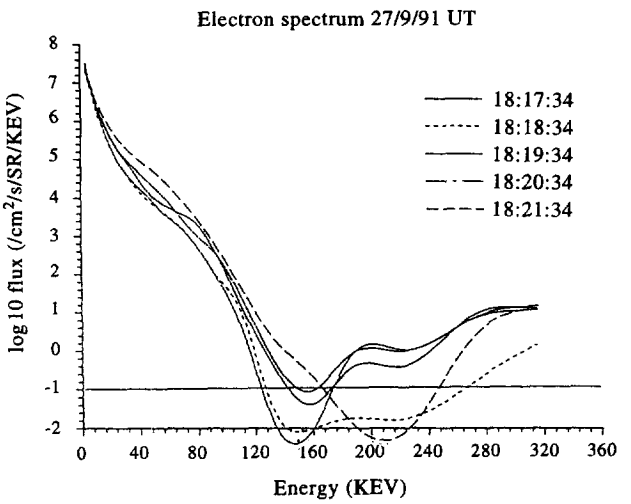

Fig. 3. Sequence of five 1 min runs of our combined model from 18:17 to 18:21 UT (19:29–19:33 LT) on 27 September 1991. This corresponds to relatively high fluxes of 'hard' precipitation and displays, in the various frames, the input density profiles, the model fits, the inferred effective recombination profiles, and the calculated flux-energy spectra. The two clearly separated parts in the spectra may be the signature of two different incoming populations.

within the 80 to 100 keV range just before the layer disappears. It seems unlikely that such spectral distributions would be the direct result of particle precipitation, although we cannot completely rule out the presence of distinctive monoenergetic peaks due to some parallel acceleration mechanism. Referring to the literature (Collis and Kirkwood, 1990, and references therein), and in the absence of other signatures in the data (in the electric field for instance), they may rather suggest the presence of long-lived metallic ions

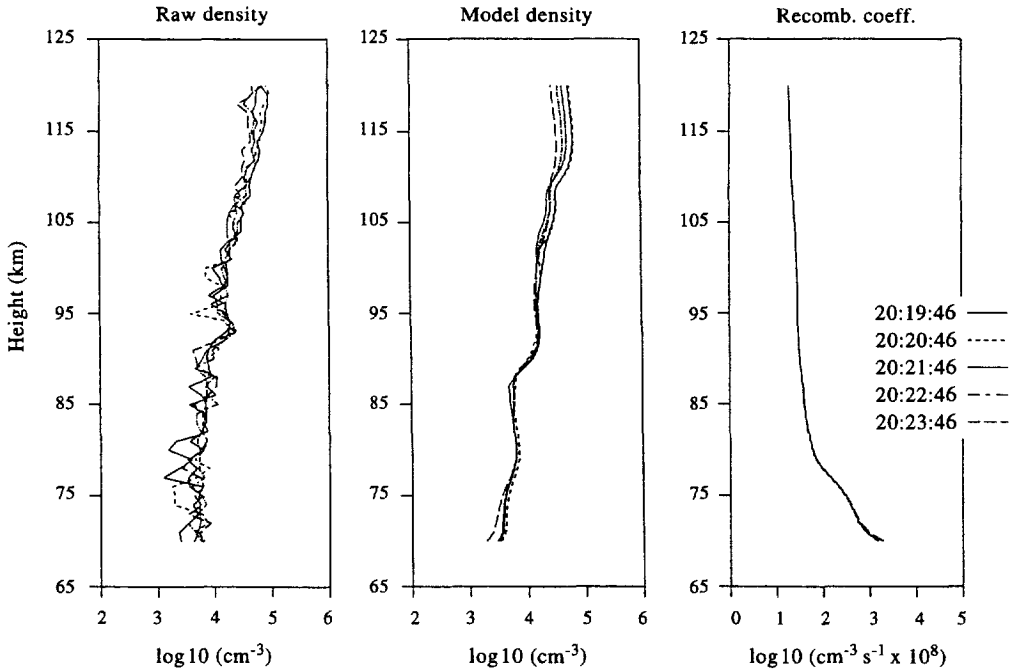

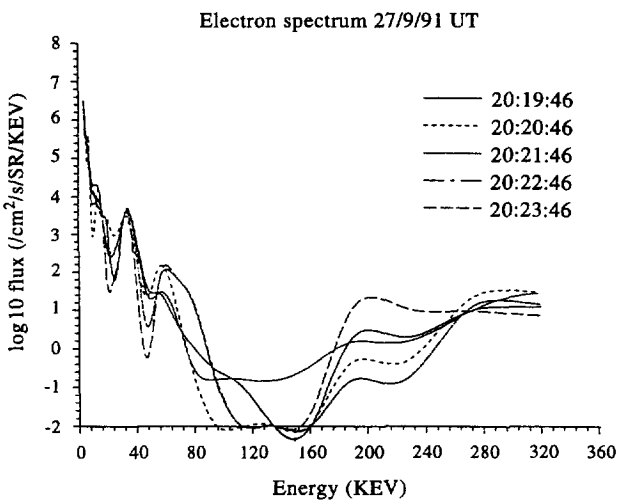

Fig. 4. Another sequence of five 1 min events in Fig. 2(b), between 20:20 and 20:25 UT (21:32–21:37 LT) on 27 September 1991. Despite the strong noise in the measured densities, both the data and the fitted profiles clearly show the presence of a sporadic E layer between 93 and 96 km. The recombination profiles show very little variability as compared to Fig. 3, whereas the particle spectra are notoriously different. The layer is associated with well defined features breaking into the spectra in the 25 to 50 keV energy range.

produced, in part, by the ablation of impacting meteors, and by charge transfer from O_2^+ and NO^+ (see Brasseur and Solomon, 1986, p. 337).

During most of the observing period on 13–14 March 1991, the total precipitation fluxes were systematically smaller than in September 1991, but there were slightly larger fluxes of harder electrons (compare lower-altitude densities in Fig. 2(b) and Fig. 2(c)). During the March 1992 experiment, ionisation was weaker or non-existent at D region heights. In Fig. 5,

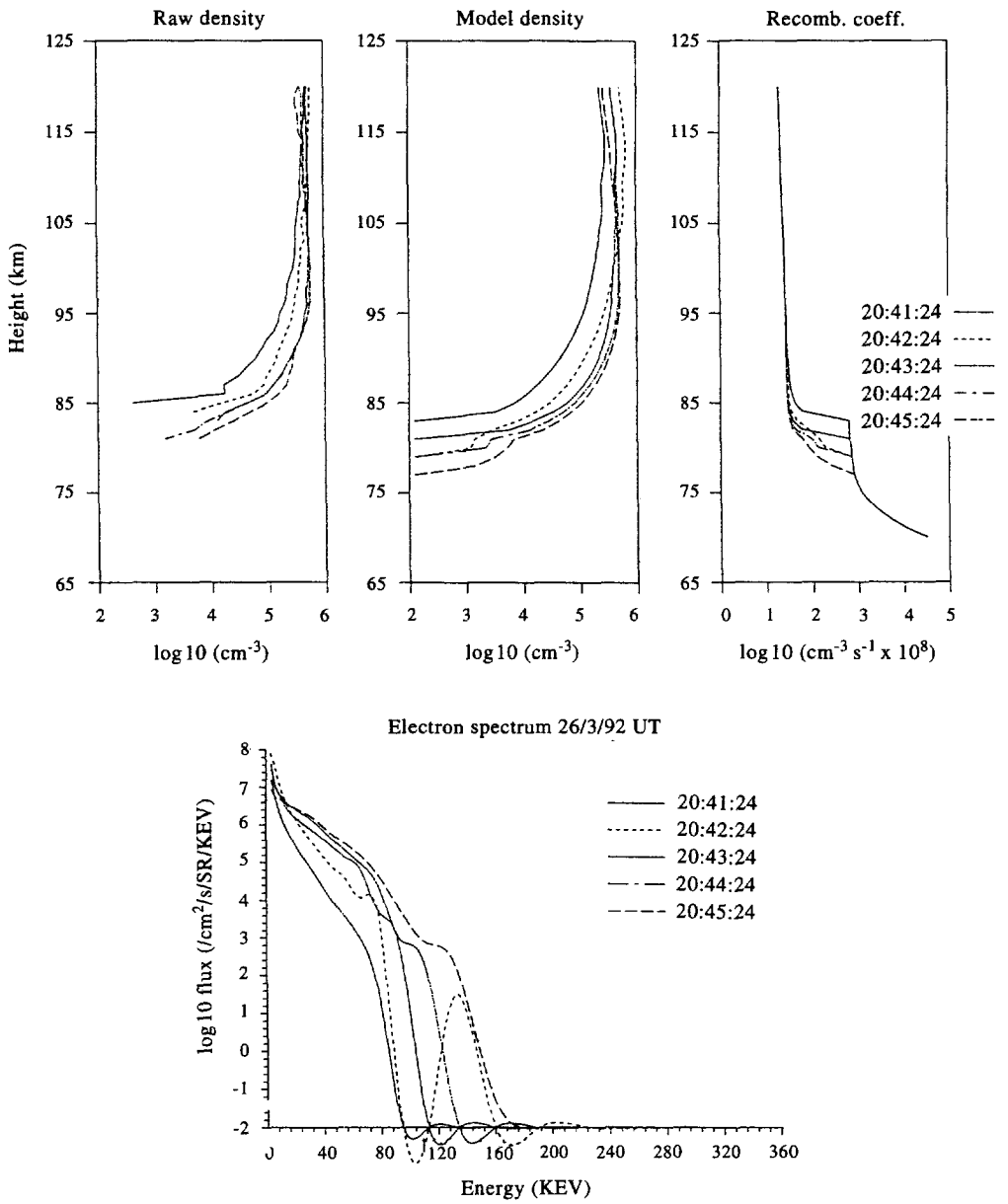

Fig. 5. This five 1 min sequence between 20:41 and 20:45 UT (21:53–21:57 LT) on 26 March 1992, shows the increasing penetration of ionisation at the lower altitudes and the corresponding increase of the precipitation fluxes in the 80 to 160 keV energy range. The fluxes are rather strong and sharply concentrated at the lower energy bands without any trace of ionisation below 80–85 km over large periods. The effective recombination coefficient is also radically affected by the flux-energy spectra of precipitation.

for instance, the five 1 min sequences between 20:41 and 20:45 UT (21:53–21:57 LT, on 26 March) show the increasing penetration of ionisation at the lower altitudes, and the corresponding increase of the precipitation fluxes in the 80 to 160 keV energy range. They correspond to relatively large precipitation fluxes concentrated mainly in the lower energy bands (see Fig. 2(a)) without any trace of ionisation below 80–85 km over large periods. Finally, Fig. 6 displays the results of 5 consecutive model runs, also from

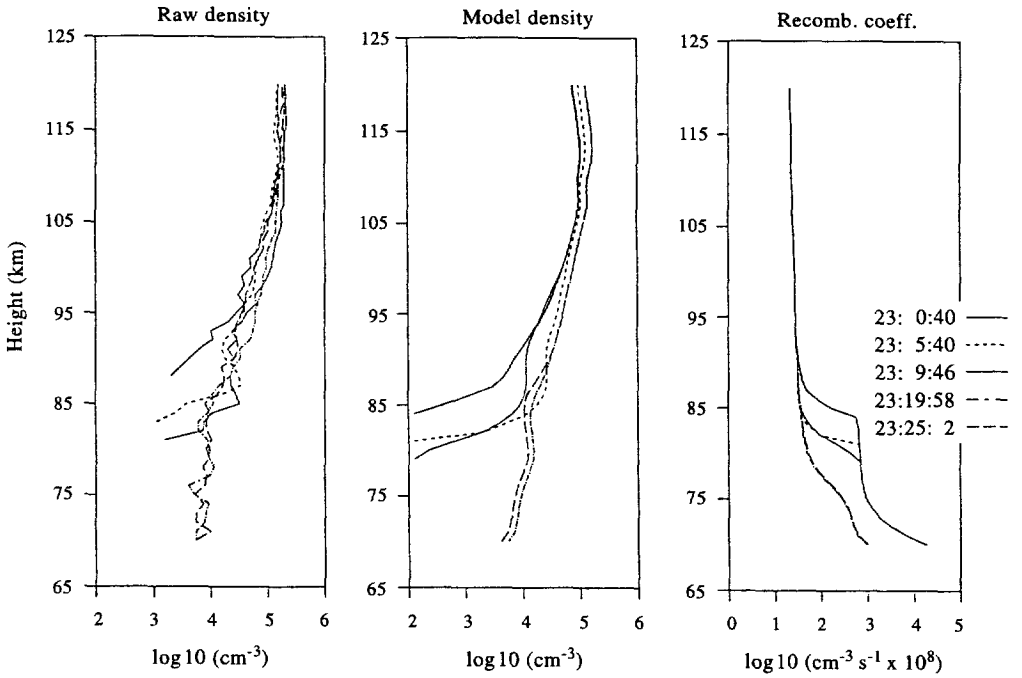

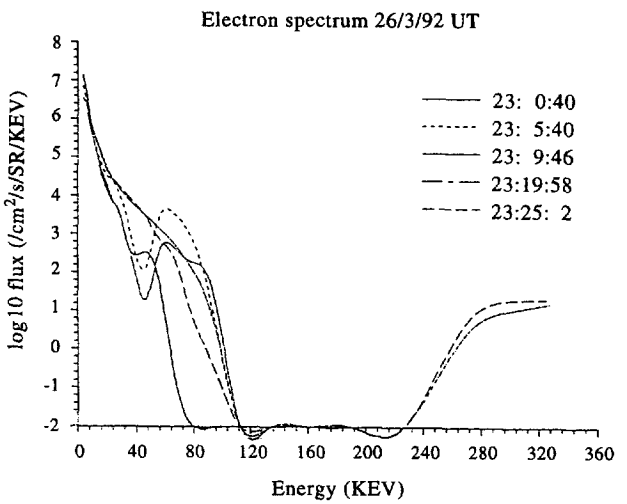

Fig. 6. Sequence of five consecutive model runs, at 5 min integration time, between 23:00 and 23:25 UT (00:12–00:37 LT) on 26 March 1992. As in previous Figures, we can verify the good agreement between the input densities and the model fits. Increasing ionisation level corresponds to increasing fluxes at higher energies, and this also produces very distinctive effective recombination profiles similar to those in Fig. 3.

the 26 March 1992 experiment but now with 5 min integration time, between 23:00 and 23:25 UT (00:12–00:37 LT). As in previous Figures, there is good agreement between the input density profiles and the model fits. The large variations in the observed density profiles, corresponding to increased precipitation fluxes at higher energies, produce large changes in the effective recombination profiles which go from shapes similar to those in Fig. 5 to those in Fig. 3. The flux intensity at the higher energies increases progressively from 23:00 to 23:25 UT, with the ionisation reaching lower into the D region. Considering the local time of

the events in Fig. 6, they could correspond to the Harang discontinuity region, and the secondary maxima in some spectra, at about 60 keV, may suggest the presence of 'drifting' Maxwellian distributions and possible field-aligned acceleration. In all cases, after approximately 03:18–04:18 UT (04:30–05:30 LT) in the September 1991 experiment, and after 03:48–04:48 UT (05:00–06:00 LT) in the two winter periods in March 1991 and 1992, precipitation production is still strong but is gradually overtaken by photoionisation.

4.2. *Recombination coefficient*

In Fig. 7, we summarize the results of our determinations of the effective ion recombination profiles(α_{eff}, in cm^3/s) and the associated average ion mass (in a.m.u.), over the entire observing periods in March 1992 and September 1991, with 1 min integration time. Contours are given as functions of height and Universal Time. The discontinuities and the very sharp variations in the contours, at the lower altitudes, occur at times when data are either absent or of poor quality. Referring to Fig. 2, during most of the March 1991 and March 1992 experiments, the integrated fluxes have comparable average values of the order of 2×10^7 electrons per cm^2 per second, whereas during the September 1991 period they are systematically greater by a factor of 10 to 20. However, as we mentioned before, ionisation at the lower altitudes in March 1991 was either comparable with or relatively stronger than in September 1991. During these two periods and for the same heights, the corresponding effective recombination coefficients are also comparable — particularly below 85 km — but the average ion mass profiles are not. Below 80 km, the relative proportion of heavier ions appears to be greater in September 1991 than in March 1991.

The large variations in the recombination coefficient and the average ion mass during the March 1992 period, as shown in Fig. 7, clearly illustrate the drastic changes in the 'cross-over' altitude between the cluster and the molecular ions due to the very dynamic nature of the lower boundary of ionisation due to relatively softer precipitation during this period. The altitude of the cross-over from cluster to molecular ions varies from about 70 to 90 km, according to season and latitude. Changes in the atmospheric temperature may accelerate the decomposition of higher order clusters and also could inhibit the process of clustering from NO^+, and these two effects will decrease the recombination coefficient (see Mitra, 1981). Below 85 km, the recombination of positive ions with electrons is faster for cluster ions than for molecular ions such as O_2^+ and NO^+ and, thus, clusters will be more efficiently destroyed in the presence of precipitation.

Figure 8 displays two extreme cases from our calculations of the effective ion recombination coefficient ((b) for strong, harder precipitation, and (a) for much weaker, less energetic fluxes), together with some average dependences from the literature (curves (1) to (4)). These summarize a large number of observations, curves (1) to (3) being taken from Gledhill (1986), and curve (4) from Vickrey *et al.* (1982). For easier visualization, we show the decimal logarithm of the recombination coefficient multiplied by 10^8. Curve (1) corresponds to a number of auroral precipitation events at night, curve (2) to nighttime events over a broad range of conditions, and curve (3) to a number of daytime observations. Values in curves (2) and (3) only apply below 90 km, and curve (4) is generally valid above 90 km. Curve (5) shows our proposed dependence for the recombination coefficient during daytime and disturbed nighttime conditions. For a given height z, the effective recombination coefficient in curve (1) is given by $\alpha_{eff} = 4.30 \times 10^{-6} \exp(-0.0242z) + 8.16 \times 10^{12} \exp(-0.524z)$. In curve (2) it is given by $\alpha_{eff} = 6.52 \times 10^2 \exp(-0.234z)$, in curve (3) by $\alpha_{eff} = 0.501 \exp(-0.165z)$, and in curve (4) by $\alpha_{eff} = 2.50 \times 10^{-6} \exp(-0.0195z)$.

The results of curve (a) for a soft precipitation event fall within the range covered by curves (1) and (2) (see Gledhill, 1986). All the cases of increasingly harder precipitation, as displayed in Figs 7 and 8, are distributed between curves (2) and (3). Our curve (b), on the other hand, falls within the range of the daytime observations for which curve (3) is the average. Our model predicts that the recombination profile limits beyond a certain level of hard precipitation. This profile is very close to the one for daytime conditions, and may be approximated by curve (5), given as follows:

$$\alpha_{eff} = 2.50 \times 10^{-6} \exp(-0.0242z) + 1.63 \times 10^{11} \exp(-0.524z). \quad (13)$$

As we may also notice in Fig. 8, curve (b) is reasonably approximated by curve (3) below 85 km, and by curve (4) above 80 km. Curve (5) may be giving a reasonable approximation to the effective recombination profile at all heights during both daytime and harder nighttime precipitation events. In Figs 5 and 6, we may see how the effective recombination coefficient is radically affected below 90 km by the flux-energy spectrum of precipitation. The sharp variation in the recombination profiles is associated with the minimum ionisation height of the incoming electrons, and delineates the boundary of the 'ground

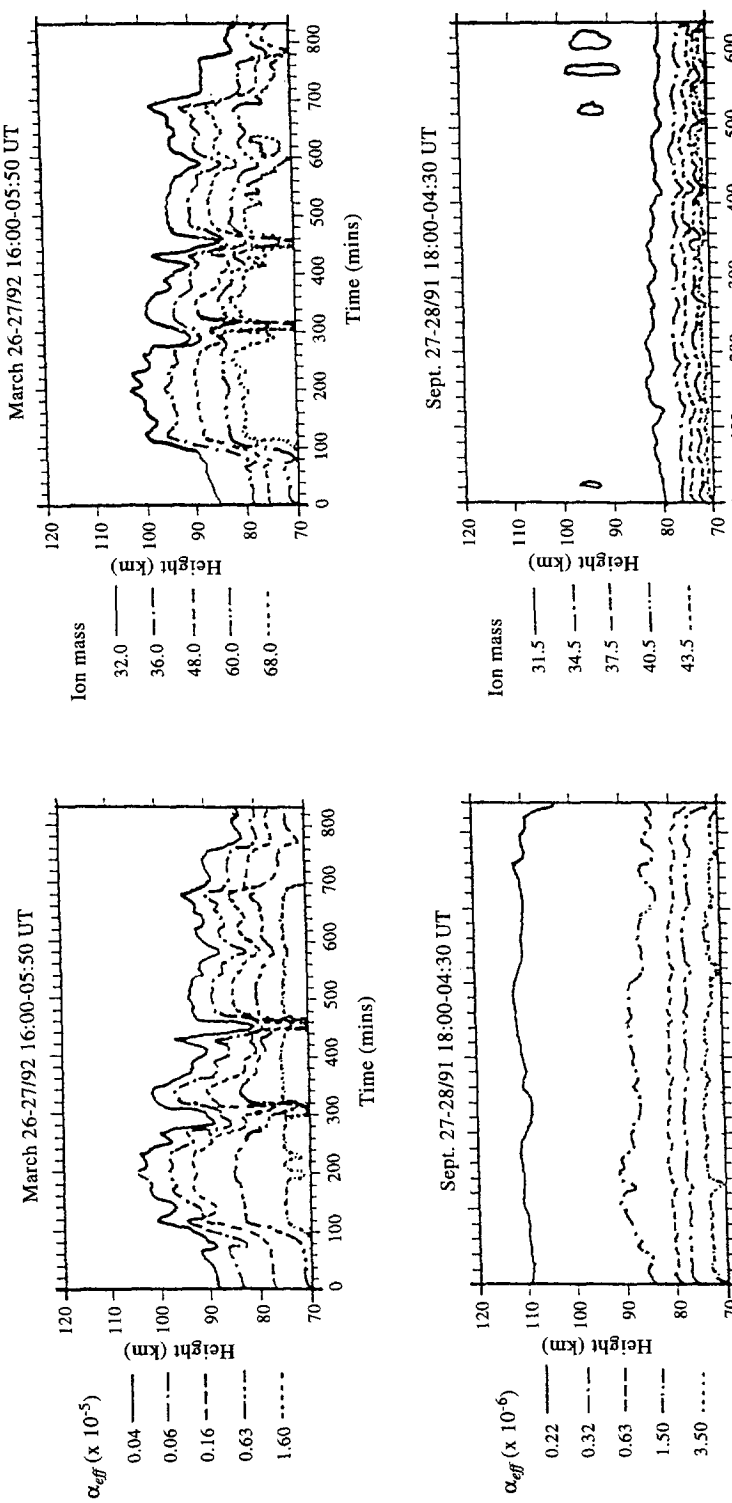

Fig. 7. Contours for the effective ion recombination coefficient (left-hand side panels) and the average ion mass (right-hand side panels) resulting from the inversion of the electron density profiles observed in March 1992 and September 1991. Contour-lines in all panels are given as functions of height and Universal Time. The recombination coefficient is given in cm^3/s, and the average ion mass in a.m.u.

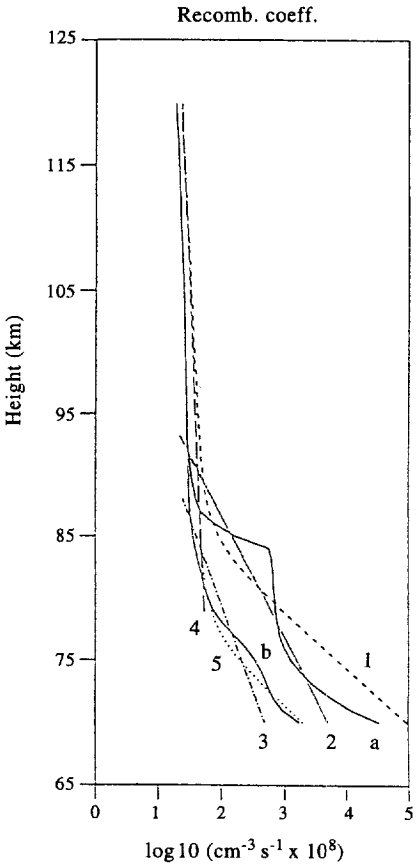

Fig. 8. Decimal logarithm of effective recombination coefficient (multiplied by 10^8) as a function of height (y-axis in km) from two extreme cases in our results ((b) for strong, 'harder' precipitation, and (a) for much weaker, less energetic fluxes), and from a number of average functional dependencies fitted to large sets of observations (curves (1) to (3), and (4)). Curve (5) shows our proposed dependence for daytime and disturbed nighttime conditions.

state' mesosphere at night (below which production is due only to cosmic ray fluxes and scattered solar radiation). The spread of the effective recombination profiles over a few orders of magnitude at the lower altitudes must be the result of the varying transition height between simple molecular ions and cluster ions. This transition corresponds to a ledge in α_{eff} down to the boundary of zero precipitation flux. Below this boundary α_{eff} changes very little in the region where cluster ions are dominant (from 85 to 77 km) and, below 77 km or so, it greatly increases with the ratio of negative ion density to the electron density.

Below 77–75 km the negative ion to electron density ratio is greater than unity and completely controls the value of α_{eff} (see equation (4)). The recombination coefficient will increase with this ratio, particularly at night when the negative ions become increasingly dominant with decreasing altitude. Negative ions are destroyed by detachment by solar radiation and through collisions with the neutral constituents, and ultimately by mutual neutralization with positive ions. In the presence of electron precipitation the relative abundance of molecular positive ions increases and recombination with negative ions becomes more efficient (see Mitra, 1981). Increasingly harder precipitation will depress the ledge in the recombination profile down to 70–75 km as chemical processes reduce the relative abundance of clusters and negative ions as compared to molecular ions. Below about 80 km (see Fig. 8) the displacement of the ledge is not complete and the recombination profile appears to reach an almost constant shape, similar to its daytime shape, during highly disturbed nighttime conditions. Comparing Figs 3–6, there seems to be a minimum flux of harder precipitation above which the recombination coefficient would be independent of the spectrum of the incoming electrons.

4.3. *Ion concentrations*

Figures 9–12 show the concentrations of the 35 ions inferred from the chemical equilibrium model, corresponding to two different precipitation spectra at 23:09 and 23:19 UT (00:21 and 00:31 LT) on 26 March 1992. In these two cases the auroral source is mainly responsible for the ionisation. At the heights of interest, the background electron density is 10 or even 100 times smaller, and basically due to the ionisation of the molecular oxygen and the nitric oxide by the diffuse Lyman-α and Lyman-β radiation. Figure 9 shows, on the left-hand side, the electron density together with the total positive-ion (I^+) and the total negative-ion (I^-) concentrations as functions of altitude; on the right-hand side, the average ion mass is also shown as a function of height. Notice that the electron density profile (e^-, full-line) and the I^+ profile (broken-line) are superimposed for most heights and only differ at the lower levels. The upper panels correspond to the event at 23:09 and the lower panels to the one at 23:19. Both the total positive and negative ion concentrations increase strongly with the electron density during precipitation (below 85 km in the Figure) and, as expected, the average ion mass is greatly reduced at the corresponding altitudes. We have not, in our present calculations, studied in detail the lifetimes of the various ions involved in the chemical equilibrium; in all cases an average lifetime is defined by the effective ion-recombination time equal to $1/[\alpha_{\text{eff}}(1+\lambda_-)n_o]$, where n_o is a long-term average of

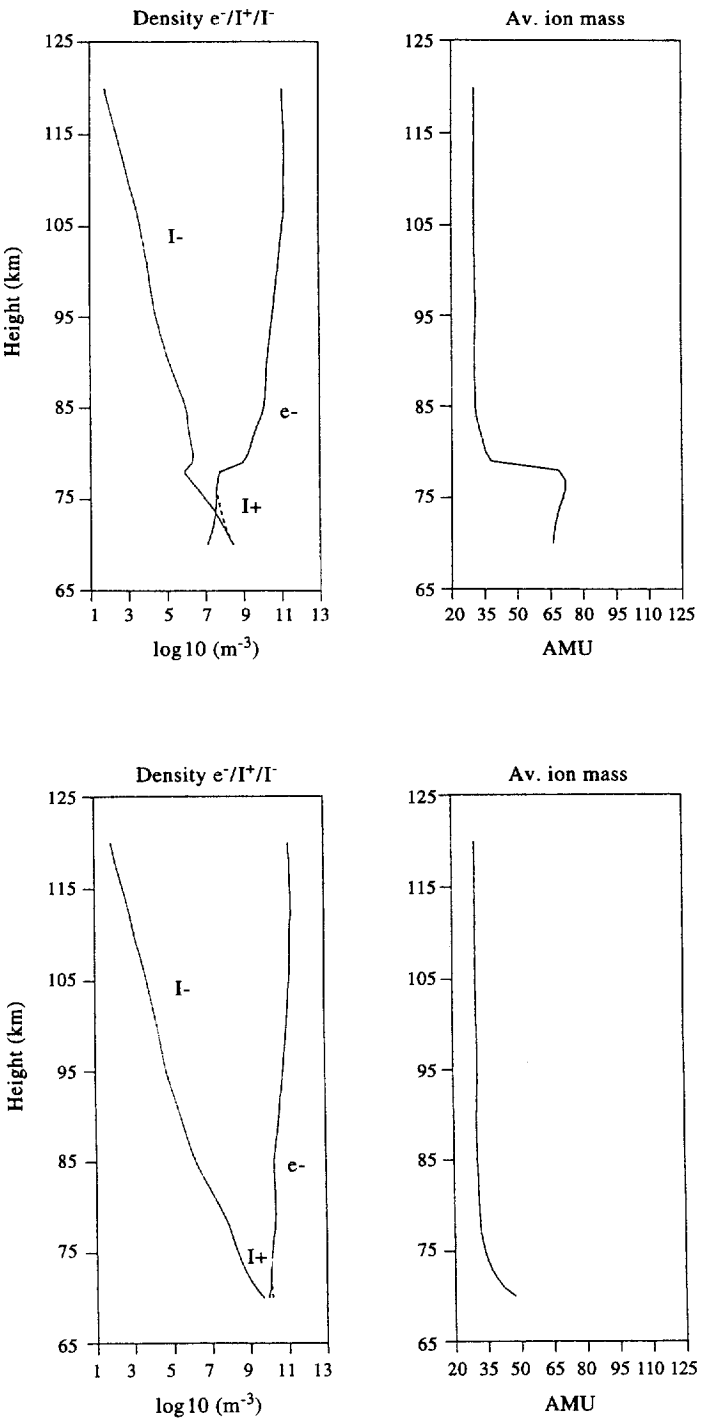

Fig. 9. The ion concentrations charge drastically between two very distinctive events in Fig. 6 (at 23:09 for the upper panels, and 23:19 for the lower panels). Displayed, on the left-hand side, is the electron density together with the total positive-ion (I^+) and the total negative-ion (I^-) concentrations as functions of altitude. On the right-hand side is the average ion mass at every corresponding height.

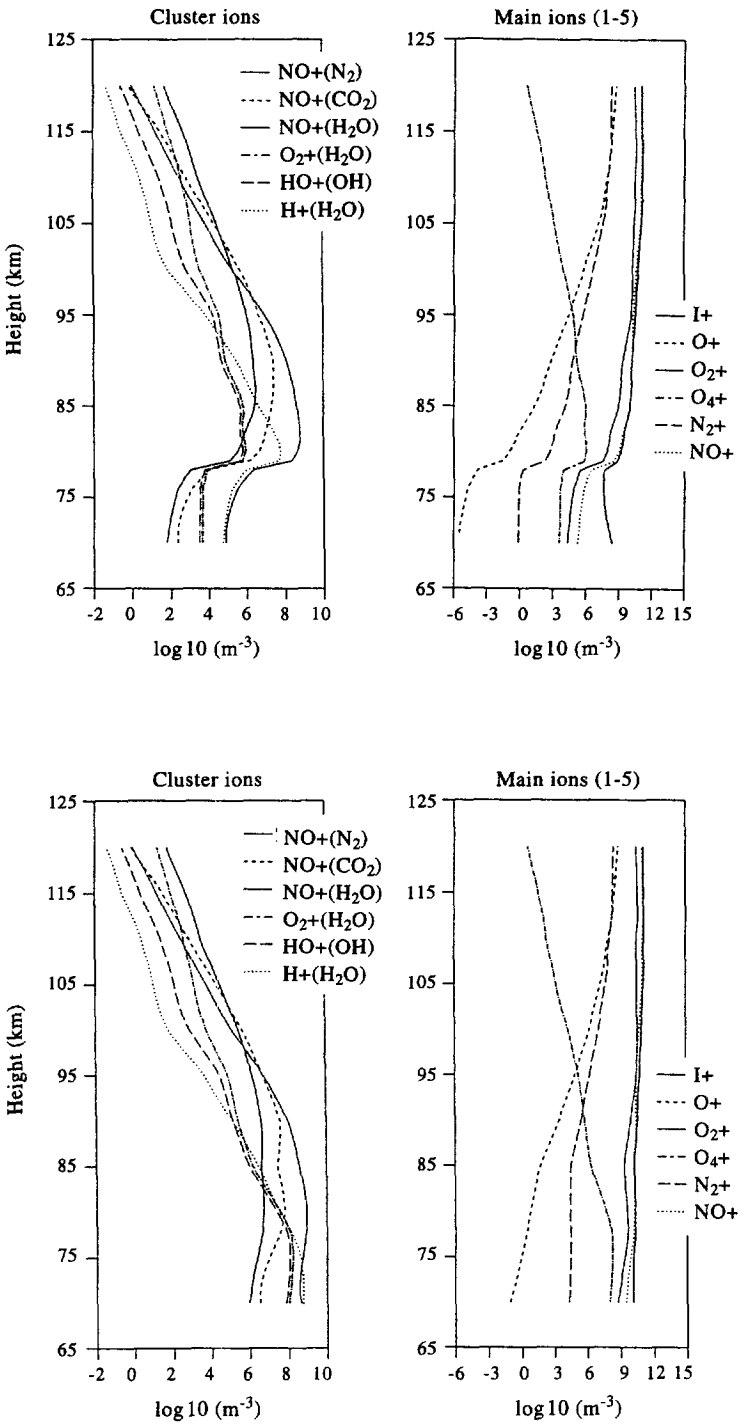

Fig. 10. Concentrations of all 24 positive ions considered by the chemical model, for the same two events as shown in Fig. 9. The upper panels in both cases correspond to the results at 23:09 and the lower panels to those at 23:19. This Figure shows, on the right-hand side, the concentrations of the five main positive ions together with the total positive-ion concentration I^+. On the left-hand side, it displays the concentrations of a number of cluster and hydrated ions.

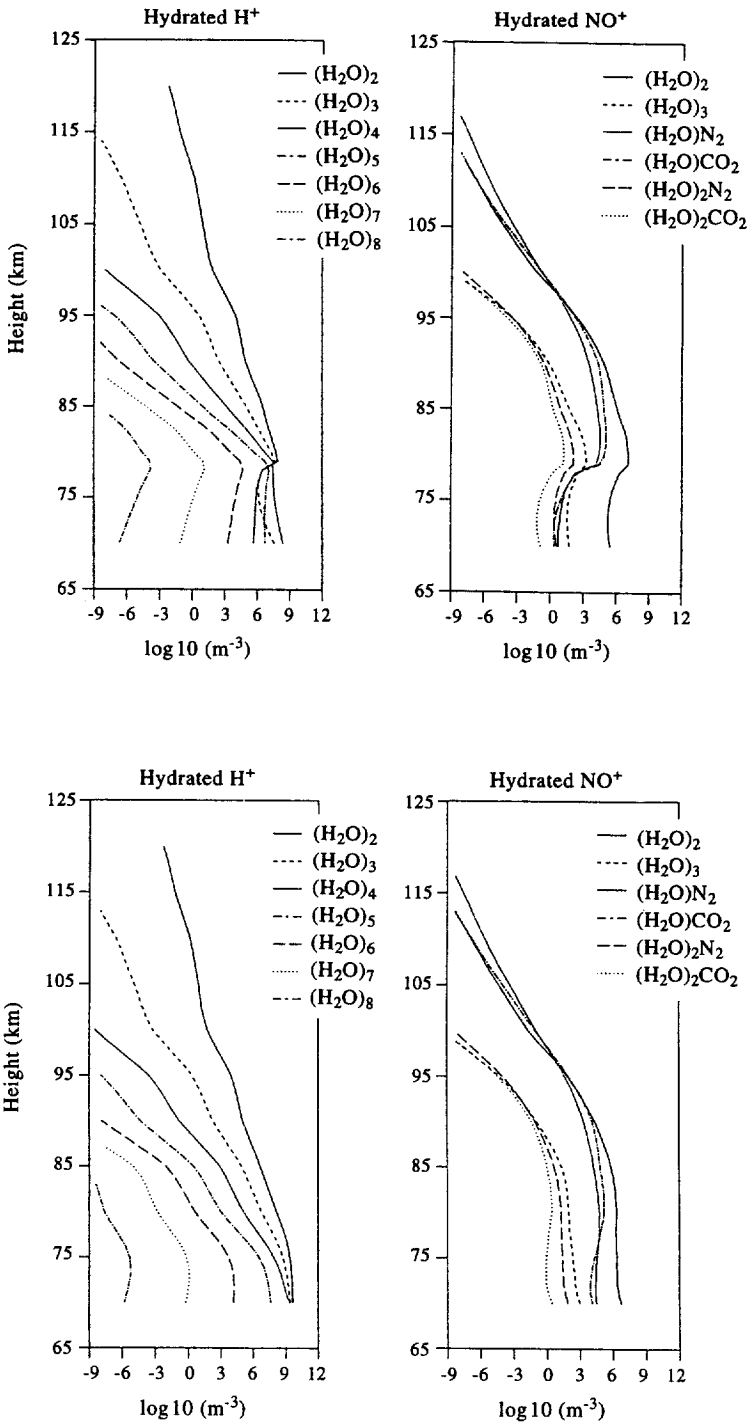

Fig. 11. Similar to Fig. 10, on the right-hand side are displayed the concentrations of hydrated NO^+-based ions, whereas on the left-hand side are those of the higher order proton hydrates. The various line-styles identify the number of water molecules or other hydrated-clusters attached to H^+ or NO^+.

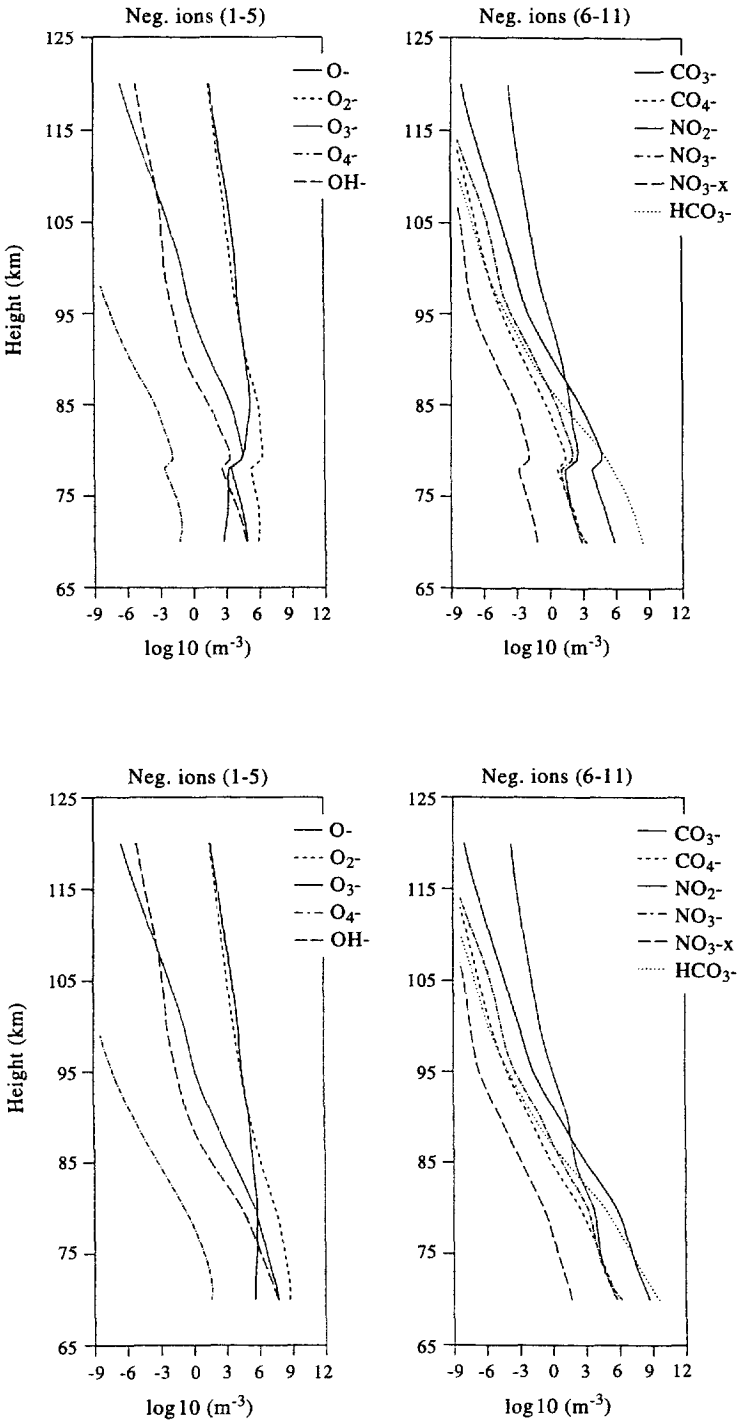

Fig. 12. Concentrations of the eleven negative ions considered by our model for the same two events considered in Figs 9–11. The upper panels correspond to the event at 23:09 and the lower panels to the 23:19 event. The two panels on the left-hand side display the concentrations of five ions, and those on the right-hand side display the concentrations of the other six ions.

the electron density. This time is shorter in the D region, ranging from some tens of seconds to a few minutes at the top E region, and it decreases with the increase of ionisation at a given height.

Figures 10 and 11 together display the concentrations of all 24 positive ions considered in the chemical model. The upper panels in both Figures correspond to the results at 23:09 and the lower panels to those at 23:19. In Fig. 12, the right-hand side panels show the concentrations of the five main positive ions (O^+, O_2^+, N_2^+, NO^+, and O_4^+) together with the total positive-ion concentration I^+. The left-hand side panels display the concentrations of a number of cluster and hydrated ions ($NO^+(N_2)$, $NO^+(CO_2)$, $NO^+(H_2O)$, $O_2^+(H_2O)$, $H_3O^+(OH)$, and $H^+(H_2O)$). In Fig. 11, on the right-hand side, we display the concentrations of hydrated NO^+-based ions ($NO^+(H_2O)_n$, $n = 2, 3$; $NO^+(H_2O)_nN_2$, $n = 1, 2$; and $NO^+(H_2O)_nCO_2$, $n = 1, 2$), whilst on the left-hand side we show the concentrations of higher order proton hydrates ($H^+(H_2O)_n$, $n = 2$ to 8). The concentration of proton hydrates up to the 3rd order is reduced between 80 and 88 km and then increased at lower altitudes, whereas the concentration of higher order hydrates is reduced below 85–88 km. The concentrations of the NO^+ hydrates are also reduced by precipitation below 88 km (down to 78–80 km).

Finally, Fig. 12 gives the concentration profiles of the 11 negative ions expected to play an important role in the chemistry of the lower ionosphere. As in the previous cases, the upper panels correspond to the event at 23:09 and the lower panels to the 23:19 event. The two panels on the left-hand side display the concentrations of five ions O^-, O_2^-, O_3^-, O_4^-, OH^-, and those on the right-hand side display the concentrations of the other six ions, CO_3^-, CO_4^-, NO_2^-, NO_3^-, NO_3^-*, HCO_3^-. We may also notice in Figs 10–12 the large increase with precipitation, generally below 80 km, in the concentrations of almost all cluster and negative ions. The apparent contradiction with the reduction in the average ion mass shown in Fig. 11 is explained by the proportionately larger increase in the concentration of molecular ions.

The equilibrium electron density below 85 km is extremely sensitive to the changes in the concentrations of both cluster and negative ions. Underestimating them will also result in the underestimation of the derived fluxes (for energies greater than 100 keV) and of the recombination coefficient. Comparisons with the summary results for α_{eff} in Fig. 8 could also indicate that, in fact, the Sodankylä chemical model may be underestimating the relative importance of negative ions, and this results in the large depletion in the α_{eff} profile which we obtain during disturbed conditions. In particular, the ion chemistry applied in this study does not consider other possibly relevant negative ions such as chloride ions Cl^-, $Cl^-(H_2O)$, ClO^-, and clusters of the form $X^-(H_2O)_n$, with X^- replaced by CO_3^- and NO_3^-.

5. CONCLUSIONS

Energetic charged particle precipitation reduces the average ion mass at a given altitude without, apparently, radically modifying the chemistry of the lower ionosphere. It increases the concentrations of most ions but also increases the relative abundance of the molecular ions. The effective recombination coefficient will change very slowly with height above 85–90 km over a broad range of precipitation levels, and its value appears to be the same as in the daytime. A unique profile, however, does not appear to exist in the D region. Below 85 km, cluster and negative ions exert a controlling influence over the variations of α_{eff}, and the spread of the effective recombination profiles over a few orders of magnitude at the lower altitudes is the result of the varying transition height between molecular and cluster ions, and the increasing importance of negative ions at the lower altitudes.

During daytime, and also during highly disturbed conditions at night, the dominance of the molecular ions over the cluster and negative ions is not complete and, particularly below 77–75 km, the large concentration of negative ions keeps the values of the recombination coefficient high, and increasing with decreasing altitude. In our determinations there also appears to be a minimum flux of harder precipitation above which the recombination profile is independent of the flux of the incoming particles and comparable to the daytime values, when the concentrations of the negative ions are at their lowest. The comparisons with results from a large number of experimental determinations of α_{eff}, as summarised from the literature, seem to indicate that our values for the effective recombination coefficient below 80 km are systematically smaller than those determinations which, in its turn, may result in the underestimation of the flux of precipitating electrons. Because of the complexity of the chemistry in this region, and the very critical role played by the negative ions, there is, indeed, a possibility that the chemical model which we use may fail to give an accurate representation of all relevant negative ions and the reactions controlling their concentrations.

Finally, the combined model does not include the transient effects of precipitation and stronger electric

fields, resulting in the heating of all the components of the plasma, and thus affecting the reaction rates and cross-sections which may favour some reactions while inhibiting others. This could produce drastic changes in the chemistry of the E and D regions. Similarly, we are not considering dynamical effects at the longer time scales and, therefore, not accounting for the expected variations in the densities of the neutral background through transport. This is especially important for NO, the basic raw material in the formation of the E and D regions. We project a follow-up study to address some of these problems by using the UCL-Sheffield model and an improved version of the Sodankylä chemical model.

Acknowledgements—We thank the Sodankylä Geophysical Institute for providing us with the initial version of their ion chemistry model. This study was commenced within the programme of D region studies at Lancaster University with a grant from the U.K. Science and Engineering Research Council, and completed at the Atmospheric Physics Laboratory at University College London with the support of the U.K. Particle Physics and Astronomy Research Council.

REFERENCES

Barouch, E. (1980) *Energy spectra of incident electrons from auroral ionisation profiles.* Note Technique CRPE/87, CNET-CNRS, Paris, France.

Basu, A., Jasperse, J. R., Robinson, R. M., Vondrak, R. R. and Evans, D. S. (1987) Linear transport theory of auroral proton precipitation: a comparison with observations. *Journal of Geophysical Research* **92,** 5920.

Berger, M. J., Seltzer, S. M. and Maeda, K. (1974) Some new results on electron transport in the atmosphere. *Journal of Atmospheric and Terrestrial Physics* **36,** 591.

Brasseur, G. and Solomon, S. (1986) *Aeronomy of the Middle Atmosphere.* D. Reidel Publishing Co., Dordrecht, Holland.

Brekke, A. (1975) The effective recombination coefficient measured in the auroral E-region during a sudden commencement electron precipitation event. *Journal of Atmospheric and Terrestrial Physics* **37,** 825.

Burns, C. J., Howarth, W. G. and Hargreaves, J. K. (1990) High-resolution incoherent scatter radar measurements during electron precipitation events. *Journal of Atmospheric and Terrestrial Physics* **3,** 205.

Burns, C. J., Turunen, E., Matveinen, H., Ranta, H. and Hargreaves, J. K. (1991) Chemical modelling of the quiet summer D- and E-regions using EISCAT electron density profiles. *Journal of Atmospheric and Terrestrial Physics* **53,** 115.

Collis, P. N., Hargreaves, J. K., Brekke, A. and Korth, A. (1986) Experimental determination of effective recombination rates in the disturbed high latitude lower ionosphere. *Annales Geophysicae* **4,** 211.

Collis, P. N. and Kirkwood, S. (1990) Discrete layers of D-region ionisation in the high-latitude ionosphere. *Advances in Space Research* **10,** 1041.

del Pozo, C. F., Burns, C. J. and Hargreaves, J. K. (1993) Dual-beam EISCAT radar observations of the dynamics of the disturbed D- and E-regions in the early morning sector. *Journal of Atmospheric and Terrestrial Physics* **55,** 1393.

Fukuyama, K. and Kofman, W. (1980) Incoherent scattering of an electromagnetic wave in the mesosphere: a theoretical consideration. *Journal of Geomagnetism and Geoelectricity* **32,** 67.

Fuller-Rowell, T. J. and Evans, D. S. (1987) Height-integrated Pedersen and Hall conductivity patterns inferred from the TIROS-NOAA satellite data. *Journal of Geophysical Research* **92,** 7606.

Gledhill, J. A. (1986) The effective recombination coefficient of electrons in the ionosphere between 50 and 150 km. *Radio Science* **3,** 399.

Hall, C., Brekke, A., van Eyken, A. P., Hoppe, U.-P. and Thrane, E. V. (1992) Incoherent scatter radar observations of the middle atmospheric response to a PCA. *Advances in Space Research* **10,** 208.

Hargreaves, J. K. (1992) *The Solar-terrestrial Environment.* Cambridge University Press, Cambridge, Great Britain.

Hargreaves, J. K. and Devlin, T. (1990) Morning sector electron precipitation events observed by incoherent scatter radar. *Journal of Atmospheric and Terrestrial Physics* **52,** 193.

Hedin, A. E. (1987) MSIS-86 thermospheric model. *Journal of Geophysical Research* **92,** 4649.

Jasperse, J. R. and Strickland, D. J. (1981) *Approximate analytic solutions for the primary auroral electron flux and related quantities.* AFGL-TR-81-0069 Environmental Research Papers, No. 730, Space Physics Division, AFGL, Hanscom, Massachusetts.

Kirkwood, S. (1988) *Spectrum — a computer algorithm to derive the flux-energy spectrum of precipitating particles from EISCAT electron density profiles.* IRF Technical Report 034, ISSN 0284-1738, Kiruna, Sweden.

Kirkwood, S. and Eliasson, L. (1990) Energetic particle precipitation in the substorm growth phase measured by EISCAT and Viking. *Journal of Geophysical Research* **95,** 6025.

Mathews, J. D. (1978) The effect of negative ions on collision-dominated Thomson scattering. *Journal of Geophysical Research* **83,** 505.

Mitra, A. P. (1981) Chemistry of middle atmospheric ionization — A review. *Journal of Atmospheric and Terrestrial Physics* **43,** 737.

Rees, M. H. (1963) Auroral ionisation and excitation by incident energetic electrons. *Planetary and Space Science* **11,** 1209.

Rees, M. H. (1989) *Physics and Chemistry of the Upper Atmosphere.* Cambridge University Press, Cambridge, U.K.

Roble, R. G. (1995) *Energetics of the mesosphere and thermosphere, in the upper mesosphere and lower thermosphere.* Geophysical Monograph 87, American Geophysical Union.

Rostoker, G., Kamide, Y. and Winningham, J. D. (1985) Energetic particle precipitation into the high-latitude ionosphere and the auroral electrojets 3. Characteristics of electron precipitation into the morning sector auroral oval. *Journal of Geophysical Research* **90,** 7495.

Schunk, R. W. and Sojka, J. J. (1995) *The lower ionosphere at high latitudes, in the upper mesosphere and lower thermosphere.* Geophysical Monograph 87, American Geophysical Union.

Strobel, D. F., Young, T. R., Meier, R. R., Coffey, T. P. and Ali, A. W. (1974) The nighttime ionosphere: E region and lower F region. *Journal of Geophysical Research* **79,** 3171.

Thomas, L. and Bowman, M. R. (1986) A study of pre-sunrise changes in negative ions and electrons in the D-region. *Annales Geophysicae* **4,** 219.

Turunen, E., Matveinen, H. and Ranta, H. (1992) *Sodankylä Ion Chemistry (SIC) Model.* Sodankylä Geophysical Observatory Report No. 49, Finland.

Turunen, E. (1993) EISCAT incoherent scatter radar observations and model studies of day to twilight variations in the D-region during the PCA event of August 1989. *Journal of Atmospheric and Terrestrial Physics* **55,** 767.

Vickrey, J. F., Vondrak, R. R. and Matthews, S. J. (1982) Energy deposition by precipitating particles and Joule dissipation in the auroral ionosphere. *Journal of Geophysical Research* **87,** 5184.

Vondrak, R. R. and Baron, M. J. (1977) A method of obtaining the energy distribution of auroral electrons from incoherent scatter radar measurements. In *Radar Probing of the Auroral Plasma*, ed. A. Brekke. Universitetsforlaget, Oslo, Norway.

Vondrak, R. R. and Robinson, R. (1985) Inference of high-latitude ionisation and conductivity from AE-C measurements of auroral electron fluxes. *Journal of Geophysical Research* **90,** 7505.

Winningham, J. D., Yasuhara, F., Akasofu, S.-I. and Heikkila, W. J. (1975) The latitudinal morphology of 10 eV to 10 keV electron fluxes during magnetically quiet and disturbed times at the 2100–0300 MLT sector. *Journal of Geophysical Research* **80,** 3148.